

PROSPECTS FOR CHARACTERIZING HOST STARS OF THE PLANETARY SYSTEM DETECTIONS PREDICTED FOR THE KOREAN MICROLensing TELESCOPE NETWORK

CALEN B. HENDERSON¹*Draft version October 21, 2014*

ABSTRACT

I investigate the possibility of constraining the flux of the lens (i.e., host star) for the types of planetary systems the Korean Microlensing Telescope Network is predicted to find. I examine the potential to obtain lens flux measurements by 1) imaging a lens once it is spatially resolved from the source, 2) measuring the elongation of the point spread function of the microlensing target (lens+source) when the lens and source are still unresolved, and 3) taking prompt follow-up photometry. In each case I simulate observing programs for a representative example of current ground-based adaptive optics (AO) facilities (specifically NACO on VLT), future ground-based AO facilities (GMTIFS on GMT), and future space telescopes (NIRCAM on *JWST*). Given the predicted distribution of relative lens-source proper motions, I find that the lens flux could be measured to a precision of $\sigma_{H_\ell} \leq 0.1$ for $\geq 60\%$ of planet detections ≥ 5 years after each microlensing event, for a simulated observing program using GMT that images resolved lenses. NIRCAM on *JWST* would be able to carry out equivalently high-precision measurements for $\sim 28\%$ of events $\Delta t = 10$ years after each event by imaging resolved lenses. I also explore the effects various blend components would have on the mass derived from prompt follow-up photometry, including companions to the lens, companions to the source, and unassociated interloping stars. I find that undetected blend stars would cause catastrophic failures (i.e., $>50\%$ fractional uncertainty in the inferred lens mass) for $\lesssim (16 \cdot f_{\text{bin}})\%$ of planet detections, where f_{bin} is the binary fraction, with the majority of these failures occurring for host stars with mass $\lesssim 0.3 M_\odot$.

Keywords: gravitational lensing: micro — planets and satellites: detection — planets and satellites: fundamental parameters — techniques: high angular resolution

1. INTRODUCTION

Microlensing is an indispensable tool for understanding exoplanet demographics due to its unique sensitivity to low-mass planets separated from their host stars by a few AU or more. This is underscored by the fact that this region roughly corresponds to the location of the snow line in protoplanetary disks, beyond which a higher surface density of solid material is thought to facilitate the growth of more massive protoplanets on shorter formation time scales (Lissauer 1987; Ida & Lin 2005; Kennedy & Kenyon 2008).

The current OGLE-IV (Udalski 2003) and MOA-II (Bond et al. 2001; Sumi et al. 2003) microlensing surveys collectively detect ~ 15 planets per year. However, converting the routinely measured mass ratio q of the lens system (planet and host star) and the instantaneous projected angular separation s into planet mass M_p and instantaneous projected semimajor axis a_\perp is difficult and requires additional information beyond the standard microlensing light curve. Efficiently doing so will be all the more important due to the influx of data from the Korean Microlensing Telescope Network (KMTNet) (Kim et al. 2010, 2011; Kappler et al. 2012; Poteet et al. 2012; Atwood et al. 2012), a next-generation network of microlensing survey telescopes that is predicted to increase the annual microlensing planet detection rate by a factor of ~ 5 (Henderson et al. 2014a, hereafter H2014a). There are two primary methods by which to determine M_p and a_\perp with minimal model dependence.

The first is by determining the microlens parallax π_E , which can be measured from the distortion in the observed light

curve due to the acceleration of the Earth relative to the light curve expected for a constant velocity (Gould et al. 1994; Hardy & Walker 1995; Gould et al. 2009). If, for a given event, this resulting asymmetry as well as the angular size of the Einstein ring θ_E can be measured, the latter typically by combining multiband photometry with a detection of finite-source effects, then the mass of the lens system can be derived from these two observables via

$$M_\ell = \frac{\theta_E^2}{\kappa \pi_{\text{rel}}}, \quad \pi_{\text{rel}} = \pi_E \theta_E = \text{AU}(D_\ell^{-1} - D_s^{-1}), \quad (1)$$

where π_{rel} is the relative lens-source parallax, D_ℓ and D_s are the distances to the lens and source, respectively, and $\kappa \equiv 4G/(c^2 \text{AU}) = 8.144 \text{ mas}/M_\odot$. This has hitherto been accomplished for 12 planetary systems, including a two-planet system (Han et al. 2013) and a circumbinary planet with mass twice that of Earth (Gould et al. 2014). There are three different ways to measure π_E , each with its own observational challenges. Satellite parallax refers to when ground-based observatories and a space telescope are separated by a long spatial base line ($\sim \text{AU}$). Orbital parallax can be measured for events with time scales that are a significant fraction of a year and requires good observational coverage. Finally, terrestrial parallax occurs when multiple observatories at different longitudes monitor a high-magnification event simultaneously with extremely high cadences. In all cases the stringent observational requirements indicate that the fraction of events for which it is possible to measure π_E is quite small.

The second is by constraining the flux of the primary lensing mass, the host star. In the case that color information and finite-source effects provide θ_E , M_ℓ can be derived by measuring the lens flux, F_ℓ , and applying a mass-luminosity relationship (Bennett et al. 2007), given a value of the extinc-

henderson@astronomy.ohio-state.edu

¹ Department of Astronomy, The Ohio State University, 140 W. 18th Ave., Columbus, OH 43210, USA

tion toward the lens. This method has been applied to only a few planetary microlensing events (e.g., Janczak et al. 2010; Batista et al. 2014), as it requires high-resolution follow-up photometry, typically in the near-infrared (NIR). However, it does *not* necessarily require waiting for the lens and source to be resolved. In fact, there are several channels through which F_ℓ can be constrained: 1) imaging the lens after it is spatially resolved from the source, 2) inferring F_ℓ by measuring the elongation of the point spread function (PSF) of the unresolved microlensing target (lens+source) as the lens and source begin to separate, 3) promptly obtaining high-resolution follow-up photometry while the lens and source are unresolved, or 4) measuring a wavelength-dependent shift of the centroid of the unresolved microlensing target, stemming from the possibility that the lens and source have different colors. There is an array of current and planned ground-based and space telescopes that will have the NIR detectors and diffraction-limited resolution θ_{FWHM} necessary to employ these methods.

Here I present the results of simulated observing programs that explore the ability to constrain F_ℓ for predicted KMTNet planet detections. I specifically investigate only items 1–3 listed above but note that measuring a color-dependent centroid shift is a useful tool and one that was successfully implemented for the first exoplanet discovered via microlensing (Bond et al. 2004; Bennett et al. 2006). I give a review of the simulations of H2014a in §2. In §3 I describe the specific facilities whose observational capabilities I consider. I provide an overview of the practical implementation of each of these three techniques as well as my approximated methodology in §4. In §5 I detail the results for each. I then discuss the effects that contaminating flux from different types of blend stars would have in §6. Finally, in §7 I explain the implications my findings have for deriving masses of the planets that will be detected by KMTNet.

2. SUMMARY OF KMTNET SIMULATIONS

The simulations of H2014a were designed to optimize the observing strategy for and predict the planet detection rates of KMTNet. There are four primary components to their methodology:

- using Galactic models to generate populations of lens and source stars with physical properties that match empirical constraints,
- populating each lens star with a single planetary companion and computing the magnification of the source star as a function of time,
- creating realistic observed light curves, and
- implementing a detection algorithm for each light curve.

Here I provide an overview of the details of each.

2.1. Galactic Model

H2014a use the luminosity function (LF) of Holtzman et al. (1998) to obtain the absolute I -band magnitude of each source star, $M_{I,s}$. Their Galactic bulge and disk density models come from Han & Gould (1995a) and Han & Gould (1995b), respectively. They draw M_ℓ from the mass function (MF) of Gould (2000), which assumes that all main sequence stars in the range $1 < M_\ell/M_\odot < 8$ have become white dwarfs (WDs),

in the range $8 < M_\ell/M_\odot < 40$ have become neutron stars (NSs), and in the range $40 < M_\ell/M_\odot < 100$ have become black holes (BHs). All objects in the range $0.03 \leq M_\ell/M_\odot \leq 0.08$ are assumed to be brown dwarfs (BDs). H2014a consider only main sequence stars as host stars of planetary systems, excluding BDs and remnants (WDs+NSs+BHs) from the underlying lens mass distribution. The extinction map they use complements the I -band data of Nataf et al. (2013) with the NIR map of Majewski et al. (2011) and Nidever et al. (2012) for the inner bulge.

2.2. Microlensing Parameters

There are four parameters that specify a microlensing event due to a single lensing mass. The first is t_0 , the time of closest approach of the source to the lens, which H2014a draw uniformly from a generic observing season. Second is u_0 , the angular distance of the closest approach of the source to the lens, normalized to θ_E . H2014a set a maximum allowed impact parameter of 3 and draw its value uniformly. The Einstein crossing time t_E is computed via

$$t_E \equiv \frac{\theta_E}{\mu_{\text{rel}}}, \quad (2)$$

where μ_{rel} is the relative lens-source proper motion. Last is ρ , the angular radius of the source star normalized to θ_E .

H2014a then populate each lens star with a planetary companion. The mass ratio q is given by

$$q = \frac{M_p}{M_\ell}. \quad (3)$$

H2014a assume a circular orbit for the planetary companion and compute s via

$$s = \frac{a}{R_E} \sqrt{1 - \cos^2 \zeta}, \quad (4)$$

where R_E is the physical size of the Einstein ring radius and ζ is the angle between the plane of the sky and a_\perp at the time of the microlensing event. Finally, α gives the angle of the source trajectory relative to the star-planet binary axis and is drawn uniformly. H2014a use these parameters to compute the magnification of the source due to the static binary lens system as a function of time.

2.3. Light Curve Generation

H2014a then convert the magnification into an observed flux. Their weather data for each KMTNet site come from Peale (1997) and they compute the brightness of the Moon using the prescription of Krisciunas & Schaefer (1991). H2014a determine the photon rate normalization and the flux measurement uncertainties for KMTNet by calibrating to OGLE-III photometry and scaling accordingly.

2.4. Detection Algorithm

Lastly, H2014a subject each simulated microlensing event to several detection criteria to determine if the planet is robustly detected. First, the $\Delta\chi^2$ of the observed light curve from its error-weighted mean flux must be greater than 500. Secondly, the light curve must have more than 100 data points and t_0 must fall within the time coverage of the light curve. Finally, the $\Delta\chi^2$ of the light curve from a best-fit single-lens model must be greater than 160. The detection rates are then normalized according to a modified version of the cool-planet mass function of Cassan et al. (2012) that has been leveled-off at $M_p = 5M_\oplus$.

3. HIGH-RESOLUTION FACILITIES AND SIMULATED OBSERVATIONAL PROGRAMS

3.1. Current Ground-based Adaptive Optics

There are several large telescopes ($>8\text{m}$) with adaptive optics (AO) systems capable of achieving diffraction-limited resolution in the optical or NIR (see §4 of Henderson et al. 2014b for an overview). Of these, microlensing planet masses derived from F_ℓ have used H -band measurements made with NACO on VLT (Janczak et al. 2010) or NIRC2 on Keck (Batista et al. 2014). I utilize the former here as a representative example and simulate its observing capabilities.

At $\lambda = 1.66 \mu\text{m}$ the full width at half maximum (FWHM) of a diffraction-limited image on the 8.2m VLT, given by $1.22\lambda/D$, where D is the telescope aperture, is $\theta_{\text{FWHM,VLT}} = 52.2 \text{ mas}$.² I use their exposure time calculator (ETC)³ to obtain the photon rate normalization, the sky background, and the scaling of the signal-to-noise ratio (SNR) with exposure time t_{exp} . For each method discussed in §4 I simulate an observing program for each lens system H2014a predict KMTNet will detect, taking the aggregate sample to be characteristic of the types and variety of systems KMTNet will find. My assumed input instrumental parameters for the simulated observing program are:

- H -band observations, balancing PSF sharpness and resolution with sky background,
- an input spectrum of an M0V star (though the choice of template spectrum has little effect on the resulting SNR or photon rate normalization),
- a laser guide star,
- the VIS dichroic, which has high efficiency for NIR observations,
- the S27 camera, which oversamples H -band slightly, and
- the FNS/HS instrument mode, which provides higher SNR for fixed t_{exp} than does DCR/HD.

I set the minimum exposure time $t_{\text{exp,min}}$ to be 20s, recommended for H -band, or whenever $\text{SNR} = 100$ is reached, and limit each observation to a maximum of 60 60s exposures. Table 1 gives the parameters for the simulated observing program.

3.2. Next-generation Ground-based Adaptive Optics

There are currently three planned extremely large telescopes ($>20\text{m}$) that will each have an AO system and a NIR imager. I select GMTIFS on GMT as my example with which to simulate an observing program because South Korea is a 10% GMT partner, making the realization of such an endeavor as is proposed here all the more feasible and probable.

The 24.5m GMT will have a diffraction-limited resolution of $\theta_{\text{FWHM,GMT}} = 16 \text{ mas}$ in H -band (McGregor et al. 2012) and a collecting area of 368m^2 , ~ 7.5 times that of VLT.⁴ To simulate an observing program on GMT I assume the same parameters as with VLT but I increase the photon rate normalization by the factor of 7.5 to account for the increase in aperture

size and modify the sky background to include the increase in collecting area as well as the decrease in PSF area, arising from the smaller pixel size. The parameters of the simulated observing program are listed in Table 1.

3.3. Next-generation Space-based Telescopes

Bennett et al. (2006) used optical HST observations to determine the mass of the first exoplanet discovered with microlensing (Bond et al. 2004). In looking forward, however, $JWST$ will provide the largest aperture yet in space at 6.5m and will use the NIR imager NIRCAM. The bigger aperture provides a smaller diffraction limit than for HST — $\theta_{\text{FWHM,JWST}} = 68 \text{ mas}$ for $JWST$'s $\lambda = 1.50 \mu\text{m}$ short-wavelength filter.

I use the $JWST$ ETC⁵ with the following instrumental parameters:

- the F150W filter, a good approximation of H -band,
- an M0V spectral distribution, and
- average zodiacal and thermal backgrounds.

I set $t_{\text{exp,min}} = 11\text{s}$ (as suggested by the user's manual, accessed via the ETC page) or whenever $\text{SNR} = 100$ is reached and again set $t_{\text{exp,max}} = 3600\text{s}$. Table 1 shows the parameters for the simulated observing program.

4. LENS FLUX MEASUREMENT METHODS

The feasibility of constraining F_ℓ for each technique explored here hinges on the relative lens-source proper motion, μ_{rel} . The distribution of μ_{rel} for the predicted KMTNet planet detections is shown in Figure 1. It peaks at $\mu_{\text{rel}} = 5.5 \text{ mas yr}^{-1}$ and falls off more steeply toward larger values of μ_{rel} . Microlensing events with lenses located in the Galactic disk generally have larger proper motions than do events arising from lenses in the Galactic bulge. The efficacy of a given observational facility to constrain F_ℓ is set by the fraction of lens systems that are resolved from their accompanying sources a fixed time Δt after the peak of the microlensing event, which is also shown in Figure 1. This, in turn, is fundamentally determined by what portion of the μ_{rel} distribution the facility is able to sample, given its angular resolution.

There are two independent ways to obtain a relation that gives M_ℓ as a function of D_ℓ . First, θ_E can be derived from a robust detection of finite-source effects from the observed microlensing light curve, which yields the angular size of the source star normalized to θ_E , and multiband photometry, from which the physical size of the source star can be determined. Assuming the source is in the bar, D_s is known to a precision equivalent to the width of the bar. Then Equation (1) simplifies to a mass-distance relation for the lens. Secondly, a measurement of F_ℓ in conjunction with a mass-luminosity relation and an estimate of the extinction toward the lens provides another technique with which to compute the mass of the lens as a function of its distance. Coupling these two methods uniquely determines M_ℓ and thus M_p . Furthermore, measurements of both D_ℓ and M_ℓ together give the physical Einstein ring radius, which can then be used to determine a_\perp .

In the case of imaging a resolved lens, it is possible to directly measure the vector proper motion from the angular separation of the lens and source, the time elapsed since the peak

² <http://www.eso.org/sci/facilities/paranal/instruments/naco/doc.html>

³ <http://www.eso.org/observing/etc/>

⁴ <http://www.gmto.org/resources/>

⁵ <http://jwstetc.stsci.edu/etc/input/nircam/imaging/>

Table 1
Parameters of Simulated Observing Programs

Facility	θ_{FWHM} [mas]	$t_{\text{exp,min}}$ [s]	$t_{\text{exp,max}}$ [s]	Collecting Area [m ²]	Object Photon Rate ^a [e s ⁻¹]	Background Photon Rate [e s ⁻¹]	Plate Scale [mas pixel ⁻¹]
NACO on VLT	52.2	20	3600	49.29	49.0	934	27.0
GMTIFS on GMT	16	20	3600	368	366	239	5.0
NIRCAM on <i>JWST</i>	68	11	3600	25	1290	4.77	31.7

^a For a point source with $H = 18$.

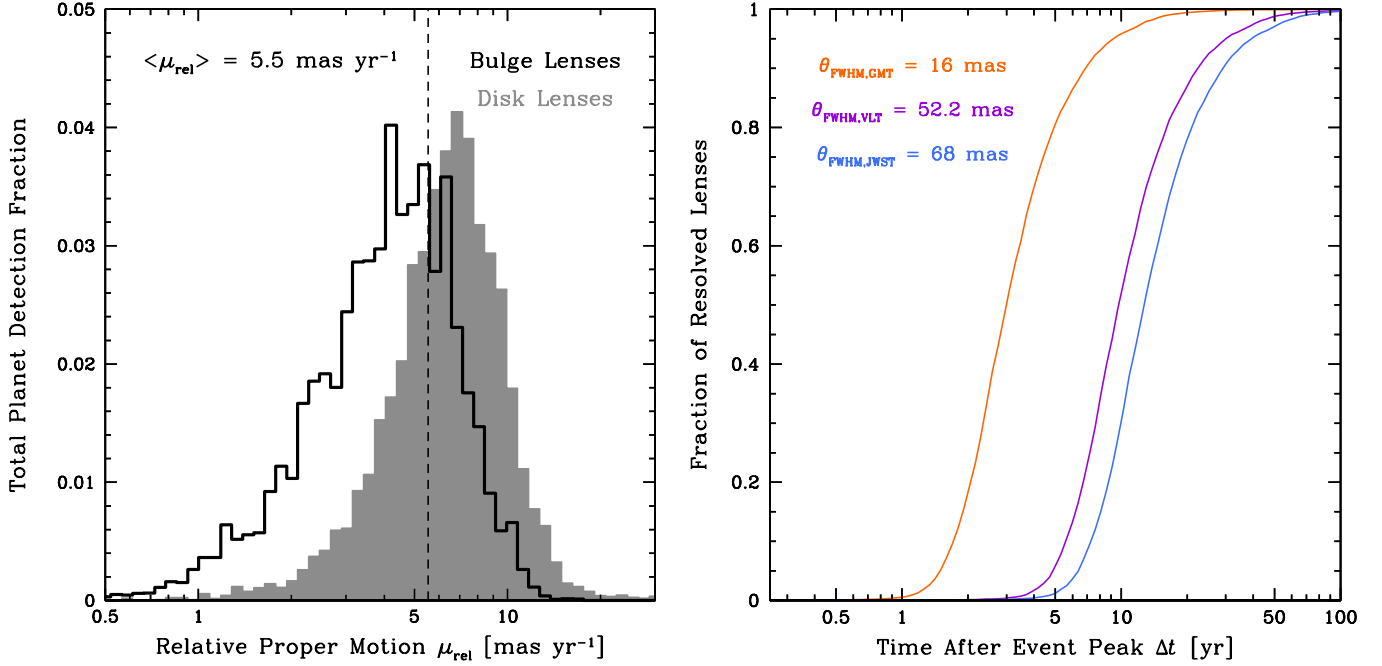


Figure 1. Distribution of relative lens-source proper motion μ_{rel} for the planet detections predicted for KMTNet (left) and fraction of lenses that will then be resolved from the source as a function of Δt for each facility (right). The fraction of microlensing events for which a given facility will be able to constrain F_ℓ depends sensitively on the fraction of events it can resolve a fixed time Δt after each event. This population is similar for VLT and *JWST*, given their comparable diffraction-limited resolutions θ_{FWHM} , but is shifted toward significantly shorter values of Δt for GMT.

of the event, and u_0 . When considering PSF elongation measurements and prompt follow-up photometry, I assume the magnitude of μ_{rel} is known from Equation (2). Then, in the case of the former, the elongation gives the flux ratio of the lens and source. The source flux is measured from the microlensing light curve, although typically in a different bandpass than is used for the high-resolution photometry, thereby providing an estimate of the source color.

4.1. Imaging a Lens Spatially Resolved from the Source

4.1.1. Practical Implementation of Technique

A lens can be directly imaged after it is spatially resolved from the source. The wait time Δt after the closest approach of the source to the lens is at least several years for typical Galactic microlensing events. This arises from the fact that it depends on both the relative proper motion of the two systems, which is generally $< 10 \text{ mas yr}^{-1}$ (see Figure 1), as well as the angular resolution attained by the observational facility, which is $\sim 100 \text{ mas}$ for current facilities with the highest resolution. In principle, after a resolved lens is imaged using a high-resolution facility, its measured apparent magnitude can be combined with a mass-luminosity relation and an estimate of the lens extinction to provide M_ℓ and, given an assumed D_s , a_\perp .

4.1.2. My Approximated Methodology

Here I take a lens to be resolved from the source when their angular separation satisfies

$$\Delta\theta_{\ell,s} \equiv \sqrt{(\mu_{\text{rel}}\Delta t)^2 + (u_0\theta_E)^2} \geq \theta_{\text{FWHM}}. \quad (5)$$

For all my simulated observing programs I assume that the minimum angular separation for the lens and source to be resolved is given by the θ_{FWHM} of that facility, which is approximately equal to the *FWHM* of an Airy Disc, given by $1.028\lambda/D$.

Next I determine the apparent *H*-band magnitude of the lens, H_ℓ . For the planetary host star of each lens system, I use the 1 Gyr isochrone of Baraffe et al. (1998, 2002) to obtain the absolute *H*-band lens magnitude, $M_{H,\ell}$, given its mass M_ℓ (see §3.1.3 of H2014a). I then convert the *I*-band extinction toward the lens, $A_{I,\ell}$ (see §3.1.4 of H2014a), to the *H*-band lens extinction, $A_{H,\ell}$, using the relations of Cardelli et al. (1989) and assuming $R_V = 2.5$ (Nataf et al. 2013). Finally, I compute H_ℓ from $M_{H,\ell}$, $A_{H,\ell}$, and D_ℓ (see §3.1.2 of H2014a).

I then simulate an observing program for each lens system that would be resolved from its source for several values of Δt . For each facility, I determine t_{exp} and *SNR* as described in their respective sections in §3. Lastly, I compute the fractional

precision to which F_ℓ can be measured in H -band, σ_{H_ℓ} , using each facility after each Δt interval.

4.2. Elongation of the PSF of the Unresolved Microlensing Target

4.2.1. Practical Implementation of Technique

It is not necessary to wait until the lens and source are spatially resolved to constrain F_ℓ . As Δt increases, the combined PSF of the unresolved lens and source will become distorted on a time scale dictated by μ_{rel} . In the regime in which $\Delta\theta_{\ell,s} < \theta_{\text{FWHM}}$, this elongation of the PSF of the microlensing target (lens+source) can be measured photometrically. But, the PSF elongation itself stems from two factors: the separation of the lens and the source as well as their brightness ratio. Thus, in order to constrain F_ℓ in this way it is necessary to obtain an independent measurement of one of these two causal parameters. The lens-source separation can be determined by measuring μ_{rel} as described in §4. Then the elongation of the PSF subsequently gives the flux ratio of the lens and source. Since the source magnitude is routinely derived from the ground-based light curve, F_ℓ can be computed (see Bennett et al. 2007 for a complete discussion). Finally, as in the case of imaging a resolved lens, combining the inferred F_ℓ with a mass-luminosity relation and an estimate of the lens extinction yields M_ℓ and also a_\perp , assuming a source distance.

It is important to note that this technique hinges sensitively on the precision to which the morphology of the PSF is known. Otherwise, any distortion of a PSF whose shape is poorly characterized could lead to a false-positive elongation measurement. While I assume perfect knowledge of the PSF here, I concede that having sufficiently precise knowledge of the intrinsic PSF for a ground-based AO facility can prove extremely challenging. This can be somewhat alleviated by the fact that typical bulge observing fields contain large samples of bright and isolated stars that can be used to model the PSF, but it may still be quite difficult to extensively model any spatial variations of the PSF.

4.2.2. My Approximated Methodology

In total there are four sources of uncertainty when using PSF elongation to constrain F_ℓ :

1. the statistical uncertainty of the source flux in the instrumental I -band, measured from the ground-based light curve,
2. the uncertainty in calibrating the instrumental I -band source brightness,
3. the uncertainty in transforming the I -band source brightness to the NIR filter of the high-resolution data, and
4. the uncertainty on the fractional lens flux.

The statistical uncertainty of the uncalibrated I -band magnitude of the source, determined from the modeling of the ground-based light curve, includes its covariances with other model parameters and is typically 2–5% (e.g., Dong et al. 2009; Janczak et al. 2010; Sumi et al. 2010; Batista et al. 2011; Yee et al. 2012). I take the typical fractional precision to be 2% to account for KMTNet’s aperture size and higher cadence. Then I take the sum of the uncertainty inherent to calibrating and transforming the uncalibrated ground-based

I -band source brightness, items 2) and 3) from above, to be a conservative 0.03 mag (Janczak et al. 2010). I note that it is possible to improve on this in cases for which ground-based H -band data were taken during the event when the source was magnified, allowing $I-H$ to be computed to $\sim 1\%$ (Batista et al. 2014).

Defining the fractional lens flux as $f_\ell \equiv F_\ell/F_{\text{tot}}$, where $F_{\text{tot}} = F_\ell + F_s$ and F_s is the flux of the source, the fractional precision of f_ℓ is given by

$$\sigma_{f_\ell} = \sqrt{\frac{2}{N_{\text{tot}}}} \left(\frac{r_0}{\Delta\theta_{\ell,s}} \right)^2 \frac{1}{|1-2f_\ell|}, \quad (6)$$

where N_{tot} is the total number of photons of the lens and source in the combined high-resolution PSF and r_0 is its Gaussian width (Bennett et al. 2007). This implies that r_0 is given by

$$r_0 = \frac{\theta_{\text{FWHM}}}{2\sqrt{2\ln(2)}}. \quad (7)$$

Computing both N_{tot} and f_ℓ requires F_s . More specifically, it requires the apparent H -band magnitude of the source, H_s . To determine H_s for each microlensing event I first use the absolute I -band magnitude of the source $M_{I,s}$ (see §3.1.1 of H2014a) and the same isochrone as in §4.1.2 to determine $M_{H,s}$, the absolute H -band magnitude of the source. While rare, it is possible that $M_{I,s} < 2.67$, the bright limit of the isochrone, in which case I assume the source is a red clump giant. I then use the absolute I -band and H -band magnitudes of the red clump, $M_I = -0.12$ (Nataf et al. 2013) and $M_H = -1.49$ (Laney et al. 2012), to derive its intrinsic $I-H$ color, $I-H = 1.37$, from which I compute $M_{H,s}$. H_s and also H_ℓ are then determined from their respective absolute magnitudes using the procedure described in §4.1.2. I similarly compute $H_{\ell+s}$, the apparent magnitude of the lens and source combined in the single PSF, from which I obtain N_{tot} . Although both f_ℓ and N_{tot} could be affected by the contaminating flux of a blend star, for these computations I assume no such contribution. In §6 I discuss the effect such a blend would have.

I subsequently simulate an observing program for each lens and source pair that would not be spatially resolved for several values of Δt . The unresolved microlensing target is treated as a single point-source object whose brightness is the combined flux of the lens and the source, $F_{\ell+s} = F_\ell + F_s$. I then use $H_{\ell+s}$ to determine t_{exp} and SNR for the respective facilities as described in §3. Finally, I compute σ_{H_ℓ} by adding Equation (6) in quadrature with the statistical uncertainty on F_s (item 1) from above) and the uncertainty in calibrating and transforming F_s (items 2) and 3) from above).

4.3. Prompt High-resolution Follow-up Photometry

4.3.1. Practical Implementation of Technique

For cases in which the lens and source are unresolved and the PSF elongation is minimal, it is yet still possible to constrain F_ℓ . Both F_s and F_{tot} are routinely measured from the ground-based microlensing light curve. Then, a high-resolution image of the microlensing target will, to a high probability, resolve out all stars not dynamically associated with the microlensing event. For reference, at the distance of the center of the Galactic bulge, $D_{\text{GC}} = 8.2$ kpc (Nataf et al. 2013), an angular separation of $\theta_{\text{FWHM,JWST}} = 68$ mas corresponds to a physical separation of 560 AU. By assuming no companions to the lens or the source, any difference between

the flux of the target measured in the high-resolution image and F_s can be attributed solely to the lens.

In practice this requires taking high-resolution observations of the unresolved microlensing target after the peak of the event, typically in the NIR, and calibrating them. The I -band flux of the source, which is routinely measured from the ground-based observed microlensing light curve data, must be transformed to the filter of the high-resolution data and also calibrated. Then, the calibrated source flux can be subtracted from the high-resolution flux of the unresolved target, and any excess light can be attributed to the lens (see §5 for a discussion of contaminating blend flux). Each of these steps — calibrating the high-resolution NIR data and transforming and calibrating the ground-based optical data — introduces uncertainty that propagates through to the excess flux measurement. A detection of the lens flux is taken to be secure only when the total uncertainty of the measured excess flux is small compared to the computed flux difference. If F_ℓ is indeed robustly detected, M_ℓ and a_\perp can be derived from a mass-luminosity relation and known values for the lens extinction and D_s .

4.3.2. My Approximated Methodology

A secure detection of F_ℓ via prompt follow-up photometry crucially requires careful treatment of the five sources of uncertainty involved in matching the ground-based and high-resolution data. In addition to items 1)–3) discussed in §4.2.2 there is

4. the statistical uncertainty of the instrumental brightness of the unresolved microlensing target (lens+source) in the high-resolution data, and
5. the uncertainty in calibrating the high-resolution measurement.

As in §4.2.2, I take the statistical uncertainty of the source flux to be 2% and the sum of the uncertainty inherent to calibrating and transforming the ground-based I -band source brightness to be 0.03 mag. The final fractional precision of the calibrated H -band magnitude of the source, σ_{H_s} , is computed as the quadrature sum of these two uncertainties.

With regard to the high-resolution data, I compute the statistical uncertainty of the flux of the unresolved microlensing target via the methods described in §3, wherein I assume the target to be a point source with flux equal to the combined flux of the lens and the source. I conservatively assign a constant 0.03 mag uncertainty to the calibration process (Batista et al. 2011) and add the two in quadrature to obtain $\sigma_{H_{\ell+s}}$. Finally, I define a lens flux detection via prompt follow-up photometry to occur when

$$\Delta H \equiv H_s - H_{\ell+s} \geq N_{\text{sig,pfp}} \times \sigma_{H,\text{tot}}, \quad (8)$$

where $N_{\text{sig,pfp}}$ represents the number of standard deviations at which the lens flux is detected and

$$\sigma_{H,\text{tot}} \equiv \sqrt{\sigma_{H_s}^2 + \sigma_{H_{\ell+s}}^2}. \quad (9)$$

5. RESULTS

5.1. Imaging a Lens that is Spatially Resolved from the Source

Figure 2 shows a cumulative distribution function (CDF) of σ_{H_ℓ} for observing programs that simulate imaging resolved lens systems $\Delta t = 1, 5, 10$, and 25 years after the microlensing events using NACO on VLT, GMTIFS on GMT, and NIR-CAM on *JWST*. Although *JWST* has the smallest aperture of

the three facilities, its extremely low background allows it to achieve $\sigma_{H_\ell} \leq 0.1$ for all lenses that are resolved from their source after a fixed Δt . Furthermore, the smaller background means the total exposure time required to do so is reduced compared to VLT and GMT. For example, given the assumptions of my simulated observing programs and using the normalized planet detection rates computed by H2014a, after $\Delta t = 10$ years it would take VLT ~ 31 hours to image ~ 25 planetary systems while it would take *JWST* only ~ 3.8 hours to image ~ 18 planetary systems, and the majority of those imaged with VLT (about two-thirds) would have $\sigma_{H_\ell} > 0.1$. The total fraction of events that can be observed after a fixed Δt with VLT or *JWST* rises as Δt increases from 5 to 10 to 25 years, stemming from the fact that their values of θ_{FWHM} are sampling the high proper motion tail ($\gtrsim 10 \text{ mas yr}^{-1}$), the peak ($\gtrsim 6$), and the low proper motion tail ($\gtrsim 2$), for those respective Δt intervals.

GMT, on the other hand, will have a collecting area ~ 7.5 times bigger than that of VLT and ~ 15 times bigger than that of *JWST*. Additionally, if GMT will be able to achieve diffraction-limited imaging in H -band, it will have a θ_{FWHM} that is ~ 3 and ~ 4 times smaller than that of VLT and *JWST*, respectively. Figure 2 shows the result of the confluence of these two factors. After $\Delta t = 5$ years, GMT’s diffraction limited resolution of $\theta_{\text{FWHM}} = 16 \text{ mas}$ allows it to resolve all events with $\mu_{\text{rel}} \gtrsim 3 \text{ mas yr}^{-1}$, or $\sim 79\%$ of the total planet detection rate. GMT would be able to measure the flux of three-fourths of those events (or $\sim 60\%$ of the total event rate) to a precision of $\sigma_{H_\ell} \leq 0.1$. Again using the normalized planet detection rates of H2014a, after $\Delta t = 5$ years GMT would be able to image the host star for ~ 51 planetary systems whose lens is resolved from the source, ~ 38 of those to a precision better than 10%, and would be able to do so in ~ 39 hours, given my assumptions for the simulated observing programs. On the other hand, after $\Delta t = 5$ years, VLT and *JWST* could image only ~ 3 and ~ 2 total planetary systems with spatially resolved lenses, respectively.

Thus, for a fixed Δt , GMT will be able to obtain direct lens flux measurements for a significantly larger fraction of predicted KMTNet planet detections than VLT or *JWST*. The primary benefit of VLT is that it exists and so could start observing lens systems shortly after KMTNet comes online, as early as the 2015 Galactic Bulge observing season, which begins in early February. The advantage of *JWST* rests in its ability to obtain $\sigma_{H_\ell} \leq 0.1$ for all lenses that are resolved after a given Δt , that its diffraction-limited capabilities do not hinge on favorable weather conditions or guide star characteristics, and the resulting shorter observing program required to image a fixed number of resolved lens systems.

5.1.1. Physical Properties of Imaged Lens Systems with High-precision Flux Measurements

I also examine the physical properties of the planet detections whose host star fluxes can be measured to a precision of $\sigma_{H_\ell} \leq 0.1$ by an example observing program. Figure 3 shows the distributions of M_ℓ and D_ℓ for spatially resolved lenses whose flux can be measured to $\leq 10\%$ for my simulated observing program using GMTIFS on GMT after $\Delta t = 5$ years. The majority of such planetary systems that will be accessible by such an example observing program reside in the Galactic disk while the remaining 42% of lens systems will be bulge lenses. In contrast, only 45% of the predicted KMTNet planet detections are expected to arise from disk lenses. This increase in the fraction of disk lenses intuitively

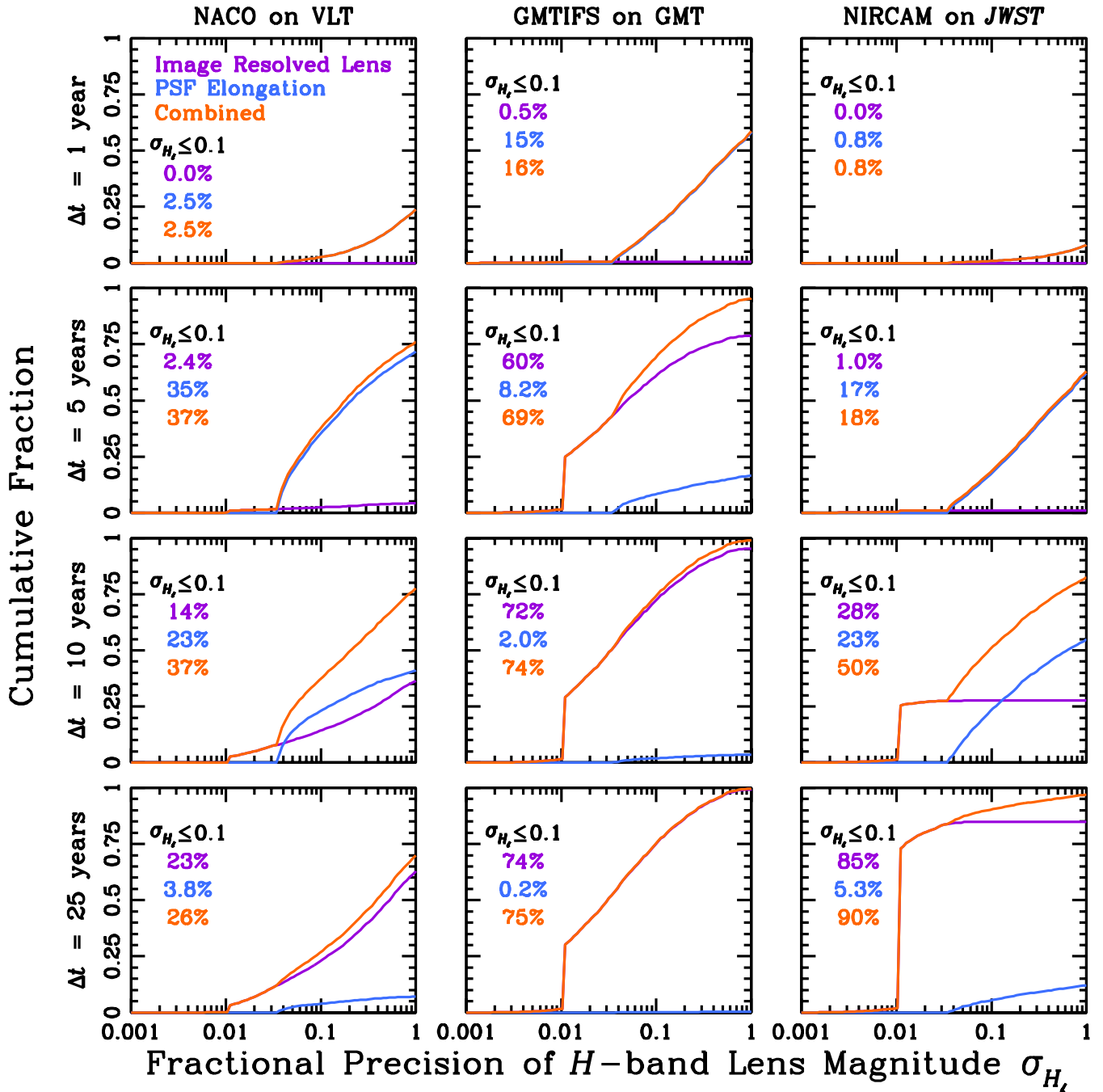


Figure 2. Cumulative distribution functions (CDFs) of σ_{H_ℓ} for imaging resolved lenses or measuring PSF elongation. The left-most column is for NACO on VLT, the middle shows GMTIFS on GMT, and the right-most NIRCAM on *JWST*. Each row represents a fixed time Δt after the peak of the microlensing event. In each figure, the curves are color-coded according to technique. GMT will be able to image a majority of resolved lenses after $\Delta t = 5$ years and *JWST* will be able to obtain $\sigma_{H_\ell} \leq 0.1$ for all lenses that are resolved after a given Δt interval. Regarding PSF elongation, GMT can constrain F_ℓ to 10% or better for approximately one-seventh of predicted KMTNet detections after only $\Delta t = 1$ year, and VLT and *JWST* can do so for $\sim 35\%$ and $\sim 17\%$ of planetary systems, respectively, after $\Delta t = 5$ years.

stems from the fact that disk lenses are generally closer, facilitating flux measurements that can be obtained with better precision. This is corroborated by the distribution of D_ℓ for spatially resolved lenses versus that for the overall KMTNet planet detection sample. The former has an average lens distance of $D_\ell = 5.6$ kpc while the latter has a mean distance of $D_\ell = 6.1$ kpc. Thus, an observing program to image spatially resolved lenses will preferentially select for closer lens systems that are more likely to reside in the Galactic disk rather

than the bulge.

Furthermore, the distributions of M_ℓ for disk and bulge lenses differ at the low-mass end. The simulated observing program predicts that precise flux measurements will be possible for stars down to the Hydrogen burning limit at $\sim 0.08 M_\odot$ for lenses in the Galactic disk. However, the least massive bulge lenses able to be imaged thusly have masses that are $\sim 50\%$ higher, around $0.13 M_\odot$. While this is to be expected, as more massive stars will be brighter, this indicates

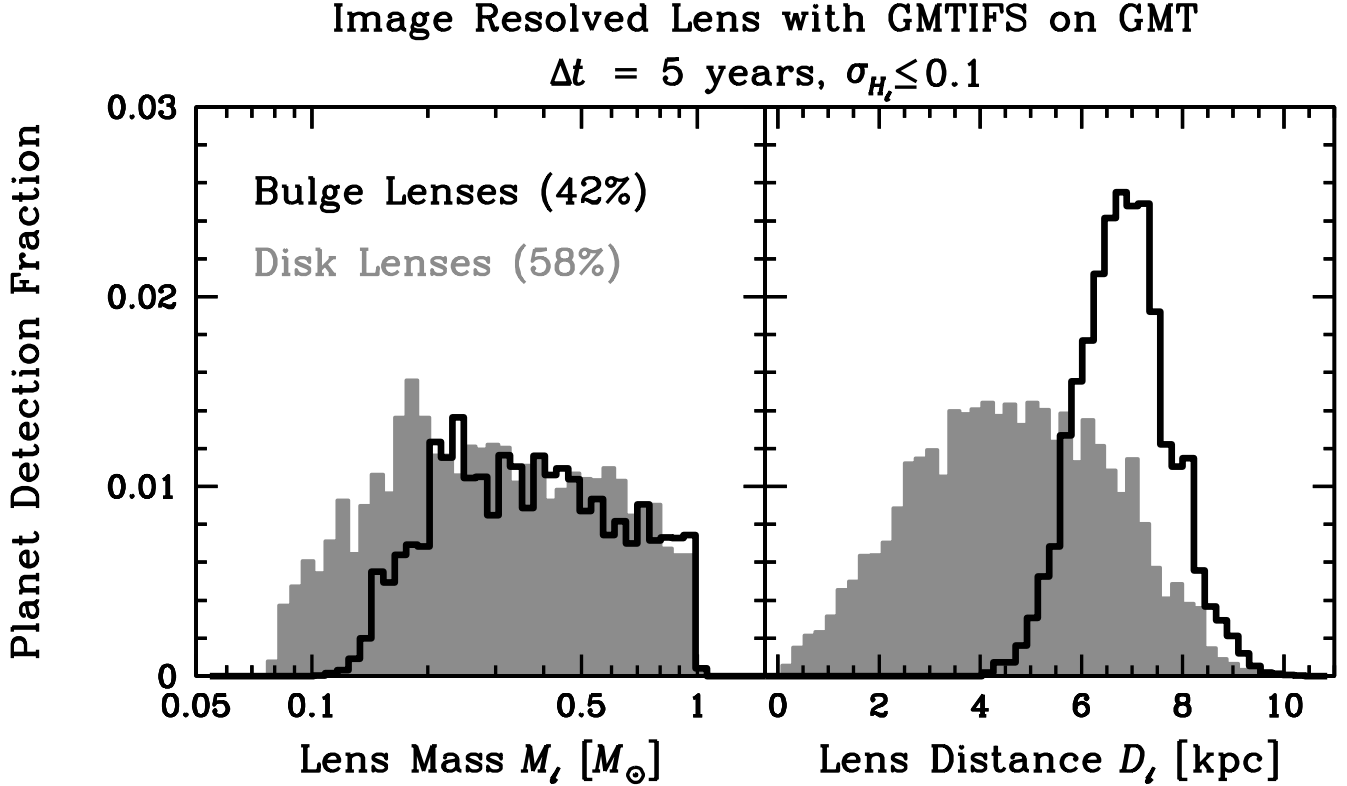


Figure 3. Distributions of M_ℓ and D_ℓ for resolved lens systems whose flux can be measured to a precision of $\sigma_{H_\ell} \leq 0.1$ using GMTIFS on GMT $\Delta t = 5$ years after each event. The fraction of disk lenses (58%) is substantially higher than the 45% of all predicted KMTNet planet detections that reside in the disk. This stems from the fact that closer lenses will be brighter for fixed M_ℓ and extinction, which is confirmed by the fact that the average lens distance is 0.5 kpc closer than the mean distance of 6.1 kpc for the full sample of predicted planetary systems. Furthermore, the disk lens population able to be imaged thusly will probe down to lower masses than will the bulge lens sample.

another implicit bias in the properties of lens systems whose masses will be derived from photometric flux measurements. Those at larger distances that generally reside in the bulge will have, on average, higher masses than nearby disk lenses, for which it will be possible to probe planetary systems whose host stars have lower mass. Understanding and accounting for these underlying selection effects when undertaking studies of the global properties of exoplanet detections will be of critical importance.

5.2. Elongation of the PSF of the Unresolved Microlensing Target

Figure 2 also shows a CDF of σ_{H_ℓ} for observing programs that estimate measuring the PSF elongation of the unresolved microlensing target for $\Delta t = 1, 5, 10$, and 25 years, again using NACO on VLT, GMTIFS on GMT, and NIRCAM on *JWST*. For GMT, after $\Delta t = 25$ years essentially all lenses and sources will be resolved given $\theta_{\text{FWHM,GMT}}$, precluding PSF elongation measurements. However, the first two terms of Equation (6) contain the implicit scaling $\sigma_{f_\ell} \propto D^{-2.5}$, where D is the diameter of the telescope aperture. Thus, not only will the elongation of the PSF of the microlensing target be more pronounced (accounting for D^{-2}), but significantly more photons of the target will be collected for a fixed t_{exp} (yielding the remaining $D^{-1/2}$). GMT is consequently able to measure F_ℓ to $\leq 10\%$ for about one-seventh of planet detections merely one year after the event. This presents a huge boon for future ground-based microlensing surveys, particularly KMTNet, and their ability to convert mass ratios q to planet masses

M_p on expeditious time scales.

5.3. Prompt High-resolution Follow-up Photometry

In Figure 4 I show the fraction of lens systems for which it will be possible to securely detect the flux of the lens as a function of planet mass M_p for three different $N_{\text{sig,pfp}}$ detection thresholds using NIRCAM on *JWST*. I consider lens flux detections with significances as low as $N_{\text{sig,pfp}} = 1$ to explore cases in which an upper limit on the brightness of the lens can be established, even if the flux measurement itself is less secure. For $N_{\text{sig,pfp}} = 1$, indicating that F_ℓ is detected at the one-sigma level according to Equation (8), it will be possible to measure F_ℓ for $\sim 42\%$ of planet detections in each mass bin. This decreases to $\sim 31\%$ for $N_{\text{sig,pfp}} = 2$ and $\sim 26\%$ for $N_{\text{sig,pfp}} = 3$. In all cases, though, it is approximately constant as a function of M_p , indicating no preference for or against certain planetary systems (as expected). Furthermore, these fractions are essentially equivalent for NACO on VLT and GMTIFS on GMT, stemming from the fact that σ_{H_ℓ} and $\sigma_{H_{\ell+\star}}$ are dominated by the uncertainties in calibrating and transforming the ground-based optical data and calibrating the high-resolution NIR data, respectively, rather than the SNR each individual facility is able to achieve.

6. POTENTIAL SOURCES AND EFFECTS OF CONTAMINATING BLEND LIGHT

In the above scenarios I have ignored the possible contributions of additional flux from stars blended with the lens and/or source. However, their presence could affect the measured fluxes and the masses ultimately derived from them. Here I

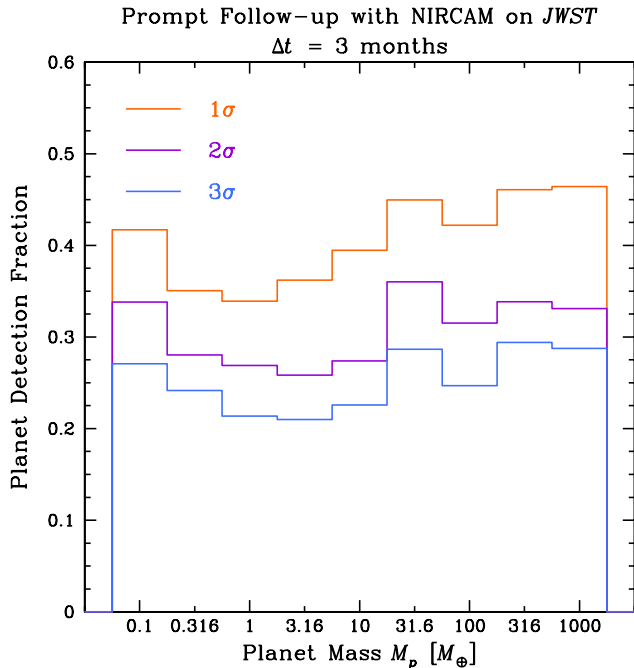


Figure 4. Fraction of planet detections in each M_p bin for which F_ℓ can be constrained via prompt follow-up photometry taken after $\Delta t = 3$ months with NIRCAM on *JWST*. The three different histograms correspond to three difference levels of significance for the lens flux detection, from Equations (8–9). The results are nearly identical for NACO on VLT and GMTIFS on GMT, given that σ_{H_s} and $\sigma_{H_{\ell+s}}$ are largely set by the uncertainties in calibrating and transforming the ground-based optical data and calibrating the high-resolution NIR data, respectively, rather than the photometric precision of each facility.

investigate the three most likely scenarios and the effect each would have.

6.1. Lens Companion

In principle, each lensing system could contain an additional stellar component whose flux could interfere with the derived value of M_ℓ . To test this, I begin by populating the lens system of each planet detection from H2014a with such a companion, all of whose parameters I will designate using the subscript “ ℓ_2 .” Here I explore the impact for prompt follow-up photometry taken $\Delta t = 3$ months after the time of the microlensing event. Even with GMT, which has the smallest θ_{FWHM} of the facilities I investigate, fewer than 0.01% of lens systems will be resolved from their source after 3 months.

6.1.1. Implementation

As described in H2014a and §2.1, the lens masses are derived from the MF of Gould (2000). I draw the mass of the companion, M_{ℓ_2} , from the same MF. If the companion is a stellar remnant or BD, which I do not exclude as viable companions, I assume it to be dark and set its apparent magnitude accordingly, $H_{\ell_2} = 30$. Otherwise, I determine H_{ℓ_2} via the procedure described in §4.1.2.

Next I determine the parameters of the binary system comprised of the primary lens mass and this companion, which I designate as ℓ_{bin} . I compute the orbital period $P_{\ell_{\text{bin}}}$ from the log-normal Gaussian distribution of Raghavan et al. (2010), which has a mean of $\log P = 5.03$ and $\sigma_{\log P} = 2.28$, where P is in days. From $P_{\ell_{\text{bin}}}$ and $M_{\ell_{\text{bin}}}$ I compute $a_{\ell_{\text{bin}}}$. I assume a circular orbit and compute $a_{\ell_{\text{bin}},\perp}$ according to

$$a_{\ell_{\text{bin}},\perp} = a_{\ell_{\text{bin}}} \sqrt{1 - \cos^2 \zeta}. \quad (10)$$

For randomly oriented orbits, $\cos \zeta$ is uniformly distributed, so I therefore draw $\cos \zeta$ from a uniform random deviate in the range $[0-1]$. The mass ratio $q_{\ell_{\text{bin}}}$ is simply M_{ℓ_2}/M_ℓ .

6.1.2. Occurrence Probability and Effect on Derived Lens Mass

In many cases it will be possible to detect the presence of a lens companion aside from its flux contribution, circumventing errors introduced by an unseen companion. The two primary ways this can be achieved are if the lens companion is spatially resolved from the unresolved microlensing target or if the source trajectory passes near enough to the central caustic that the perturbations to the caustic induced by the presence of this additional lensing mass are then observed in the light curve. To determine the former I compute the angular separation of the lens companion and the unresolved microlensing target, $\Delta \theta_{\ell+s,\ell_2}$, after $\Delta t = 3$ months and presume the companion would be detected if $\Delta \theta_{\ell+s,\ell_2} \geq \theta_{\text{FWHM}}$.

Regarding the latter, I assume the lens companion would be detected if the source passes over or very near the central caustic perturbation induced by the companion’s presence, specifically if $u_0 \leq u_{\text{cc},\ell_2}$. For a two-body lens system there exists a set of 1–3 closed caustic curves, depending on the angular separation of the lensing masses, that identify the locations in the plane of the source where the magnification of a point-like source diverges to infinity. There is one central caustic that is located near the center of mass of the lens system and 1–2 planetary caustics. I first compute the topology of the ℓ_2 binary (Erdl & Schneider 1993), which determines the total number of caustics. For all topologies I take u_{cc,ℓ_2} to be the size of the central caustic along its longest dimension. In the case of a resonant topology, for which the central caustic is the sole caustic, I compute u_{cc,ℓ_2} numerically. If the topology is close or wide, I find the approximate dimensions of the central caustic analytically using Equations (22–23) or (9–10) of Bozza (2000), respectively.⁶

I show the fraction of lens companions whose presence would be detected via the above methods in Figure 5. Here I have also excluded events whose lens and source would be resolved after $\Delta t = 3$ months with *JWST* (as a conservative estimate) as well as those for which the lens flux would not be detected at the one-sigma level or better (see §4.3), again via *JWST* (though the choice of facility doesn’t affect this criterion, as discussed in §5.3). This leaves $\sim 57\%$ of planet detections, which is roughly one-third higher than what is presented in Figure 4. The inclusion of a companion to the lens increases the flux of the non-source term in Equation (8), in turn increasing ΔH and, consequently, the overall fraction of systems for which non-source flux would be robustly detected. For those cases in which the lens companion would be spatially resolved from the unresolved microlensing target, I have not included its flux contribution when determining if non-source flux is robustly detected. Of this $\sim 57\%$, lens companions for about half of these events, or $\sim 32\%$ of all planet detections, will go undetected, with comparable fractions of companions being spatially resolved or detected by the source passing sufficiently near the portion of the central caustic for which the presence of the companion will manifest itself in the light curve.

For the $\sim 32\%$ of lens systems in which ℓ_2 is undetected,

⁶ The third term in Equations (9–10) of their manuscript contains ρ_i^2 , where ρ is their nomenclature for projected separation, when they should instead read ρ_i^3 as a result of their perturbative analysis. I have corrected this prior to my implementation of said analytic approximations.

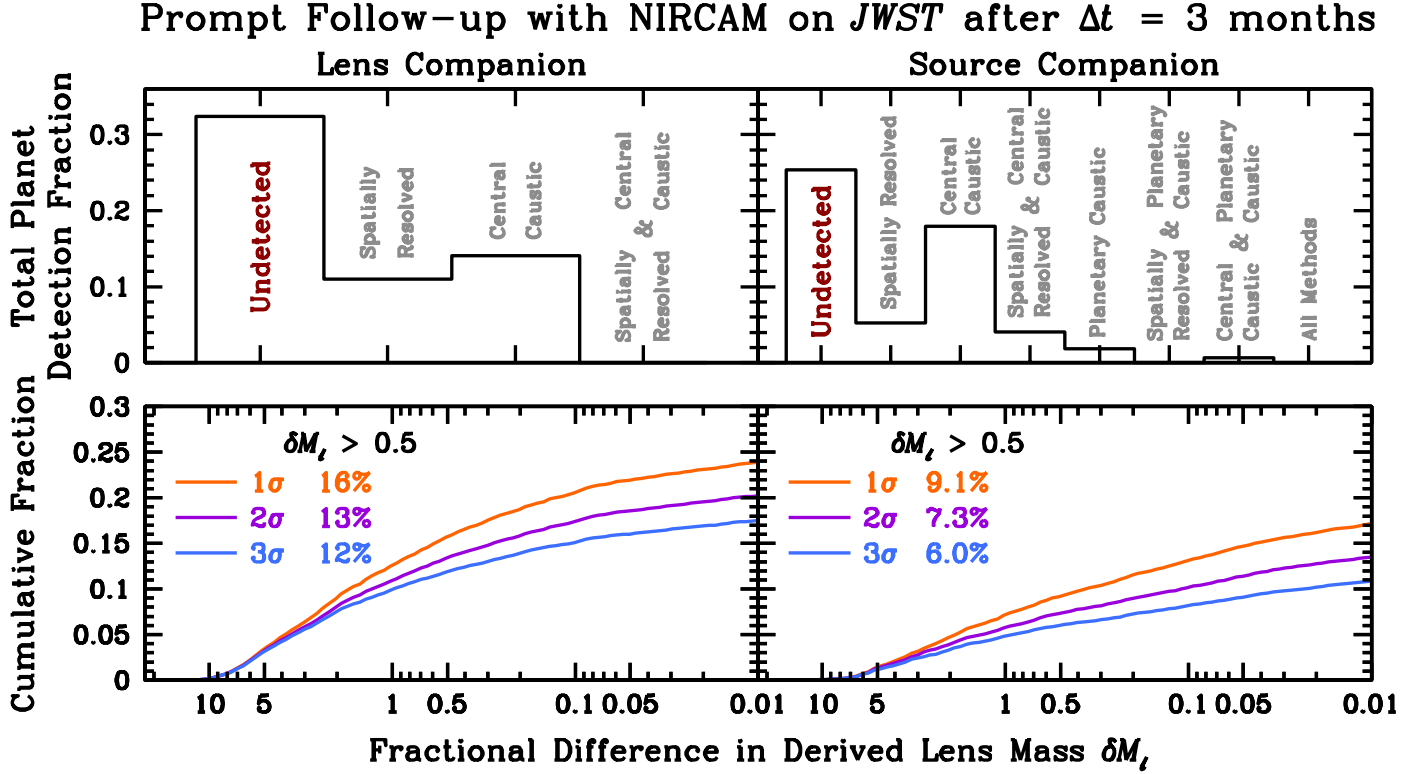


Figure 5. Detectability of lens (top left) and source (top right) companions and their respective resulting δM_ℓ CDFs (bottom). Assuming every lens or source has a companion, the companions to approximately half of the events with robust non-source flux detections will go undetected. However, the fraction of catastrophic failures in the derived values of M_ℓ is low, not exceeding $(16 \cdot f_{\text{bin}})\%$ of all planet detections, where f_{bin} is the binary fraction. This is then furthermore suppressed by empirically determined binary fractions, which are a steep function of spectral type and can be as low as $f_{\text{bin}} \sim 25\%$ for M stars (Lada 2006).

I estimate the fractional uncertainty the blend flux from this undetected companion introduces to the derived lens mass. I compute $M_{H_{\ell+\ell_2}}$, the absolute magnitude of the combination of the lens and its companion, from D_ℓ , A_{H_ℓ} , and $H_{\ell+\ell_2}$. Using the same isochrone as in §4.1.2 I determine $M_{\ell,\text{blend}}$, the mass of the primary lens that would be inferred if the blend flux contributed by the companion were undetected and otherwise attributed to the lens. I then compute the absolute fractional difference between the true primary lens mass and the mass determined when including blend flux from the undetected lens companion,

$$\delta M_\ell = \frac{|M_\ell - M_{\ell,\text{blend}}|}{M_\ell}. \quad (11)$$

Figure 5 shows the resulting CDF of δM_ℓ for three different values of $N_{\text{sig,pfp}}$.

The CDF has been truncated at $\delta M_\ell = 0.01$, which explains why the right-most limit is lower than the height of the “Undetected” bin, for two reasons. First, this threshold is comparable to the finest steps in stellar mass of the isochrone. Secondly, of the 32 planets that have hitherto been detected via microlensing,⁷ all mass values have fractional uncertainties greater than 4%, indicating that a $\sim 1\%$ uncertainty is an appropriate floor for the precision with which it is currently possible to obtain M_p for microlensing planet detections. I take $\delta M_\ell > 0.5$ to define lens systems for which there is a catastrophic failure in the determination of M_ℓ due to contaminating flux from an undetected companion to the lens. After excluding systems whose lens and source are resolved, whose

non-source light is not detected at one sigma or better, and lens companions whose presence would be otherwise noticed, either by being spatially resolved or via perturbing the central caustic, I find $\lesssim 16\%$ of lens systems will have their masses severely mis-estimated with $\delta M_\ell > 0.5$.

Figure 6 shows the fraction of lens systems with undetected lens companions as a function of the true lens mass. On average, $\sim 30\%$ of lenses with a given mass will be potentially subjected to flux contamination from a lens companion. There is a strong dependence on M_ℓ when considering only systems whose mass derivations are subject to catastrophic failures from these undetected companions. The bulk of detections with $\delta M_\ell > 0.5$ have $M_\ell \lesssim 0.3 M_\odot$ and none have $M_\ell \gtrsim 0.7 M_\odot$. Lenses with the lowest masses will have more massive companions that are thus more luminous, leading to a higher probability of significant contamination from the blend flux. Conversely, lenses near the high-mass end of the MF will generally have lower-mass companions. The mass-luminosity relation is sufficiently steep that the light from the lower-mass companions to these massive lenses will not significantly skew the derived lens mass.

For this calculation I have assumed that each primary lens star has exactly one companion (in addition to the planet). However, not only is the binary fraction, f_{bin} , $< 100\%$, but it also depends steeply on spectral type (e.g., Duquennoy & Mayor 1991; Fischer & Marcy 1992; Lada 2006; Raghavan et al. 2010 and references therein). In fact, M stars, which comprise the bulk of the Galactic lens population, can have a binary fraction as low as $\sim 25\%$ (Lada 2006). While Figure 6 shows contamination fraction as a function of M_ℓ , I allow for lens companions that are more massive

⁷ From <http://exoplanet.eu> as of 8/September/2014

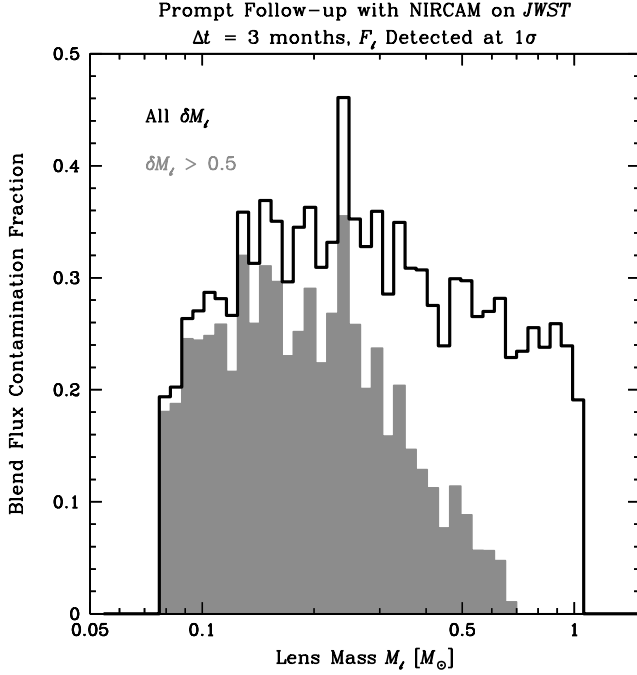


Figure 6. Fraction of lenses subjected to contamination from the blend flux of undetected lens companions as a function of M_ℓ . For derived lens masses that suffer from catastrophic failures, with $\delta M_\ell > 0.5$, there is a steep dependence on M_ℓ .

than the planet host star. In these cases the host star would not be the primary star of the stellar binary. Thus, although the higher fraction of catastrophic lens mass derivation failures for low-mass lenses is caused by brighter, higher-mass lens companions, it is these companions — *not* the lens host stars themselves — that are the primary bodies in the stellar binaries, and as such they will have different values of f_{bin} . Digesting any potential bias in the distribution of photometrically derived lens masses is thus quite complicated and will likely require a global approach rather than being addressed system-by-system.

Whatever the value of f_{bin} , it is crucial to also note that the CDF in Figure 5 will be suppressed by that same factor. This establishes the results presented here as an upper limit. Therefore, while individual systems may yet experience catastrophic failures in their mass determinations, this indicates that undetected lens companions will have a small net effect on derived values of M_ℓ for the statistically large samples of planet detections H2014a predict KMTNet will find.

6.2. Source Companion

Another possibility hitherto unaccounted for is the contribution of additional flux from a companion to the source star. As with a lens companion, if the presence of such a star goes undetected, its flux will skew the derived value of M_ℓ . Here I populate the source star of each detected planetary microlensing event predicted for KMTNet from H2014a with a companion, designating all of its parameters with the subscript s_2 . I again investigate the resulting effect only for prompt follow-up photometry $\Delta t = 3$ months after the time of each microlensing event.

6.2.1. Implementation

I determine the mass of the source companion, M_{s_2} , and its apparent H -band magnitude, H_{s_2} , following the prescription

described in §6.1.1. However, prior to obtaining the parameters of the binary source s_{bin} , I must determine the mass of the source star itself. I draw its absolute I -band magnitude $M_{I,s}$ from the LF of Holtzman et al. (1998) (see §3.1.1 of H2014a), which I use in conjunction with the same isochrone as previously to obtain M_s . If $M_{I,s} < 2.67$, the bright end of the isochrone, M_{s_2} is taken to be $1.1M_\odot$, typical for G and K giants. With the masses of both components of s_2 in hand, I compute the binary parameters $P_{s_{\text{bin}}}$, $a_{s_{\text{bin}}}$, $a_{s_{\text{bin}},\perp}$, and $q_{s_{\text{bin}}}$ as laid out in §6.1.1.

6.2.2. Occurrence Probability and Effect on Derived Lens Mass

I investigate three channels through which a companion to the source can be detected. As with a lens companion, the simplest is if the source companion and the microlensing target are spatially resolved. If $\Delta\theta_{\ell+s,s_2} \geq \theta_{\text{FWHM}}$ after $\Delta t = 3$ months I assume the companion to be detected.

Otherwise, I assume that the source companion would be detected if the source passes over the central caustic created by the lens host star and planet. In this regime $q \ll 1$, so I make use of analytic approximations for the size of the central caustic, depending on the topology. If it is a resonant topology, I compute $u_{\text{cc},\ell}$ numerically. Otherwise, if it is a close or wide topology, I use Equations (10–11) of Chung et al. (2005) (or, equivalently, Equations (24–25) of Han 2006). If $u_0 \leq u_{\text{cc},\ell}$, I assume the source companion would be detected via additional features in the light curve.

In many cases, however, the trajectory of the source will cause it to maintain a wide separation from the lensing star throughout the duration of the event (see Figure 23 of H2014a). The detection of the planet then arises from the source passing near or over (at least) one of the planetary caustics. Just as the presence of a source companion would manifest itself through extra magnification structure in the light curve as it passes over the central caustic, so would it if it were to pass over a planetary caustic, if $a_{s_{\text{bin}},\perp}$ were sufficiently small. There are no planetary caustics for a resonant topology. For a close topology I approximate the size of the planetary caustic $u_{\text{pc},\ell}$ using Equations (3), (15), and (18) of Han (2006), noting that the caustic width along the axis parallel to the planet-star separation vector is always larger than the width along the perpendicular direction, obviating computation of the latter. If it is a wide topology I compute $u_{\text{pc},\ell}$ from Equation (8) of Han (2006). If the angular separation of s_2 normalized to θ_E is smaller than the size of the planetary caustic, $\Delta\theta_{\ell+s,s_2}/\theta_E \leq u_{\text{pc},\ell}$, I assume that the source companion would induce detectable perturbations on the light curve.

In principle it is also possible to detect the presence of a source companion due to a shift in the observed color of the microlensing event. Gravitational microlensing is itself achromatic. However, in the case of a binary source it is likely that the flux ratio of the two components will deviate from one, indicating a difference in color between the two stars. Then, a microlensing target whose total observed flux is color-dependent evinces the binarity of the source, which is more readily detectable as the binary source passes over or near the caustics. While this effect has previously been measured (Hwang et al. 2013), I do not consider it here and instead mention it as an additional tool with which source companions can be detected.

Figure 5 shows a histogram of the fraction of events whose companions to the source would be detected by combinations of the methods described above. Similar to the consideration for lens companions, I include only events that remain unre-

solved after $\Delta t = 3$ months and for which the lens flux would be detected at the one sigma level or better via prompt follow-up photometry using NIRCAM on *JWST*. This represents a more conservative approach, given that the smaller values of θ_{FWHM} for VLT and GMT cause them to spatially resolve more companions from sources. I again note that the sum of the histogram bins gives a fraction that is larger than the one-sigma fraction shown in Figure 4, arising from the increase in ΔH (Equation (8)) that is due to the increase in brightness of the non-source term. Approximately 25% of source companions would go undetected, smaller than the $\sim 32\%$ of lens companions.

If the source companion is indeed undetected, then its contributed blend flux will influence the derived value of M_ℓ . I then follow the same procedure as in §6.1.2 to compute δM_ℓ . The resulting CDF is shown in Figure 5, again truncated at $\delta M_\ell = 0.01$. Even fewer undetected source companions would induce catastrophic failures in the eventual lens mass determination, with $\lesssim 9\%$ of detections having $\delta M_\ell > 0.5$. Additionally, the same caveat regarding the binary fraction f_{bin} applied to lens companions holds here, which would only further reduce the fraction of planetary systems for which prompt follow-up photometry would ultimately produce values of M_ℓ that would be catastrophically skewed. However, it is important to note that the source stars of microlensing events have spectral types that are, in general, earlier than those of lens stars, leading to different binary fractions between the two populations.

6.3. Ambient Interloping Star

I lastly investigate the probability that a star not dynamically associated with the microlensing event could be blended with the microlensing target, even in a high-resolution image. This has previously been estimated on a case-by-case basis for individual planet detections (Dong et al. 2009; Sumi et al. 2010; Janczak et al. 2010; Batista et al. 2011). The approach taken is to count the number of stars on the high-resolution image within, e.g., 3σ of the detected excess flux and estimate the probability that there could be one within the PSF of the microlensing target. While the probability of such an occurrence has been $\lesssim 5\%$ in all cases, a blend contribution from an ambient interloping star could be more insidious. Rather than the possibility that *all* of the excess flux could be due to an interloper, there exists the possibility that only some of it is. Depending on the magnitude of the contribution, this could affect the derived lens mass in the same way as an undetected companion to the lens or source.

I begin by appending the LF of Zheng et al. (2004) to that of Holtzman et al. (1998), normalizing the former to the latter using data in the range $6.5 \leq M_I \leq 9.0$, where the two overlap. Then I convert the combined LF, which now extends to $M_I = 13.5$, to H -band using the same isochrone as in §4.1.2, again using $I - H = 1.37$ for stars with $M_I < 2.67$. I take $A_I = 2.0$ to be typical of the proposed KMTNet fields (see Figure 13 of H2014a) and convert to H -band using the Cardelli et al. (1989) relations and $R_V = 2.5$ (Nataf et al. 2013) to obtain $A_H = 0.8$. Assuming a uniform distance to all interloping stars equivalent to the Galactocentric distance, $D_{\text{int}} = R_{\text{GC}} = 8.2$ kpc (Nataf et al. 2013), I then compute the CDF for $\theta_{\text{FWHM}, \text{JWST}}$, as it has the smallest aperture and thus largest θ_{FWHM} of the facilities explored here. I also multiply the stellar number density of the LF by a factor of 1.25 to account for the average increase in the surface density of stars of the KMTNet fields compared to that of Baade’s Window, for

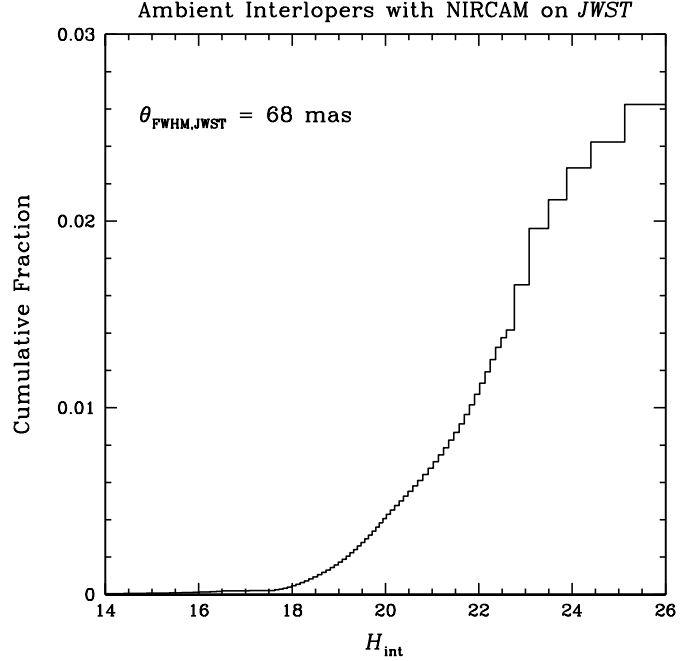


Figure 7. CDF of chance alignment with an ambient interloping star of magnitude H_{int} . A pessimistic approximation of $\theta_{\text{FWHM}} = 200$ mas increases the maximum probability to $\sim 23\%$, while a best-case scenario of $\theta_{\text{FWHM}, \text{GMT}} = 16$ mas reduces it to $\sim 0.15\%$.

which the LF was derived, using the Galactic density models described in §3.1.2 of H2014a.

6.3.1. Results

Figure 7 shows a CDF of the probability of the presence of an ambient interloping blend star as a function of H -band magnitude of the interloper H_{int} as computed above. The apparent magnitude distribution extends to $H_{\text{int}} \sim 26$, which is equivalent to the faint limit of lenses that could be detected by any of the methods discussed here. The probability of such a star falling within a seeing disc with $\text{FWHM} = \theta_{\text{FWHM}, \text{JWST}}$ is $\lesssim 3\%$ across the full magnitude range. Decreasing the assumed values of A_H and D_{int} only acts to shift the distribution to brighter magnitudes, leaving the maximum probability unaffected. In assuming $\theta_{\text{FWHM}} = 200$ mas as a worst-case scenario approximation, the CDF reaches a maximum probability of $\sim 23\%$. While this is undoubtedly more significant, it is still low and otherwise improbable, and even for smaller values of D_{int} and $A_{H, \text{int}}$ the net effect, i.e., the resulting δM_ℓ , is likely non-catastrophic. More optimistically, using $\theta_{\text{FWHM}, \text{GMT}}$ yields a maximum probability of $\sim 0.15\%$.

7. DISCUSSION

Here I have explored the potential of current and future high-resolution facilities to obtain flux measurements of the host stars of planetary systems predicted to be detected by KMTNet (H2014a). GMTIFS on GMT provides a powerful tool with which to constrain lens fluxes. It will be able to measure F_ℓ to $\lesssim 10\%$ for $\sim 60\%$ of KMTNet’s predicted planet detections $\Delta t = 5$ years after each event by imaging lenses spatially resolved from the source, and for roughly one-seventh of detections after $\Delta t = 1$ year by measuring the elongation of the PSF of the unresolved microlensing target (lens+source). Furthermore, NIRCAM on *JWST* would be able to carry out high-precision ($\sigma_{H_\ell} \leq 0.1$) measurements for $\sim 28\%$ of events

$\Delta t = 10$ years after each event by imaging resolved lenses, and NACO on VLT could obtain lens flux measurements via prompt follow-up photometry for the $\sim 42\%$ of planet detections accessible to it at the one-sigma level within $\Delta t = 3$ months of the events and could be used as soon as KMTNet comes online. These are exciting prospects for increasing the number of well-constrained microlensing planet detections, which themselves are integral to our understanding of their underlying demographics and formation mechanisms.

I additionally explore the effects contaminating flux from possible blended objects would have on F_ℓ . Undetected companions to the lens would lead to catastrophic failures in the derived lens mass, $\delta M_\ell > 0.5$, for $\lesssim (16 \cdot f_{\text{bin}})\%$ of predicted KMTNet planet detections. The same fraction for undetected companions to the source drops to $\lesssim (9 \cdot f_{\text{bin}})\%$. In both cases I have assumed 100% binarity, so these fractions would be further suppressed by the underlying distribution of stellar multiplicity. The integrated probability of blend flux contributions from interloping stars not dynamically associated with the event is even lower, reaching a maximum of $\sim 3\%$ for $\theta_{\text{FWHM,JWST}} = 68$ mas.

7.1. Measuring Lens Masses with Parallax and Proper Motion

In this paper I have focused on methods to constrain lens fluxes. By combining measurements of F_ℓ and θ_E with a mass-luminosity relationship and an estimate of the extinction toward the lens, M_ℓ can be derived via Equation (1). It is possible to also obtain an independent measurement of the lens mass from information obtained when imaging a resolved lens. Because the lens and source are resolved, their angular separation $\Delta\theta$ can be computed from the photometric images. The time elapsed since the peak of the microlensing event Δt is also known. From these two parameters the vector heliocentric proper motion can be measured. The direction of proper motion is parallel to the parallax vector. So, a measurement of the vector proper motion combined with a one-dimensional measurement of the component of the microlens parallax that is parallel to the direction of the Earth's acceleration, $\pi_{E,\parallel}$, yields a direct measurement of M_ℓ (Gould 2014).

There are several advantages to this method. It does not rely on a detection of finite-source effects, it does not require multiband data, it is not subject to the systematic uncertainties inherent in the conversion of a source color to a physical radius, and the presence of a companion to the lens and/or source does not introduce additional uncertainties (in fact, it is precisely the opposite if said companions are bright).

Here I explore the ability of a simulated observing program on GMT $\Delta t = 5$ years after each event to compute the vector proper motion and $\pi_{E,\parallel}$, which ultimately give a direct measurement of M_ℓ . There are three quantities involved in this process: 1) the magnitude of the proper motion, 2) the direction of the proper motion, and 3) the one-dimensional parallax. Given that Δt will be known to extremely high precision, the two primary sources of uncertainty will be from the vector proper motion and $\pi_{E,\parallel}$. As shown in Gould et al. (2003), the asymmetry induced by parallax can be encapsulated in a single parameter γ that is proportional to $\pi_{E,\parallel}$. They provide an analytic scaling relation⁸ to estimate the fractional precision

to which γ can be determined from a dedicated ground-based microlensing observational campaign,

$$\frac{\sigma_\gamma}{|\gamma|} = \frac{1}{12} \left(\frac{\sigma_{\text{ph}}}{0.01} \right) \left(\frac{f}{144 \text{ day}^{-1}} \right)^{-1} \left(\frac{S}{3} \right) \left(\frac{\tilde{v}}{800 \text{ km s}^{-1}} \right) \times \left(\frac{t_E}{20 \text{ days}} \right)^{-3/2} \left(\frac{|\cos \psi \cos \phi|}{0.5} \right)^{-1}, \quad (12)$$

where σ_{ph} is the photometric precision of the target, f is the cadence of observations, S will vary monotonically between 2.1 and 4.4 for typical KMTNet observations, \tilde{v} is the relative lens-source velocity projected onto the observer plane, $\cos \psi$ gives the length of the Earth-Sun separation projected onto the plane of the sky, and ϕ is the angle between the source trajectory and said projected separation. I determine σ_{ph} for each event as described in §3.3.2 of H2014a (excluding noise due to the Moon and to unresolved stars) and estimate f to be 54 day^{-1} , assuming an average nine-hour observing night and a ten-minute cadence for KMTNet's three telescopes. I take S to be 3 and compute \tilde{v} for each event via

$$\tilde{v} = \frac{\theta_E D_\ell}{t_E} \left(\frac{D_s}{D_s - D_\ell} \right). \quad (13)$$

Lastly, I set the final term equal to the fiducial value of 0.5 for each event.

I assume that the fractional precision of the magnitude of μ_{rel} is the quadrature sum of the precisions to which the centroids can be determined for both the lens and the source, which I approximate as the ratio of the FWHM (in pixels) to the SNR, divided by Δt . The uncertainty in centroiding both the lens and the source is included twice, once for each component axis. The fractional precision of the direction of μ_{rel} is similar to the fractional precision of its magnitude, so I multiply the latter by $\sqrt{2}$ to obtain the fractional precision of the vector proper motion. Because the vector proper motion measurement comes from the high-resolution data, the SNR for both the lens and source is computed as described in §3.2.

In practice, the fractional precision of a lens mass derived in this manner requires careful treatment of the covariances between all input parameters. Furthermore, the measured proper motion vector is derived in a heliocentric reference frame whereas $\pi_{E,\parallel}$ and Δt are in a geocentric frame. Transforming between the two requires solving a quadratic equation and can thus lead to a potential two-fold degeneracy in certain cases (see Gould 2014 for a complete discussion). However, as shown in Figure 8, the fractional precision of the vector proper motion from the high-resolution data is generally much better than that of γ . I thus assume that the latter will set the minimum fractional precision of M_ℓ and show its distribution in Figure 8. Even taking this to be a conservative lower limit, only $\sim 14\%$ of events would have $\sigma_\gamma/\gamma \leq 0.1$, and $\sim 40\%$ would have $\sigma_\gamma/\gamma > 0.5$. Nevertheless, photometric follow-up of microlensing events by groups such as the Microlensing Follow-Up Network (Gould et al. 2006) and RoboNet (Tsapras et al. 2009) provide high-cadence coverage that can increase f in Equation (12) by up to an order of magnitude.

I graciously acknowledge B. Scott Gaudi for his support, patience, and insightful comments. I also thank Matthew T. Penny, David M. Nataf, and Andrew P. Gould for stimulating discussion, Susan Appel for her loving support, Richard

⁸ Their manuscript indicates that $\sigma_\gamma \propto f$ when it should read $\sigma_\gamma \propto f^{-1}$, i.e., a higher observational cadence acts to improve the precision to which γ can be measured. I have corrected this in the above equation.

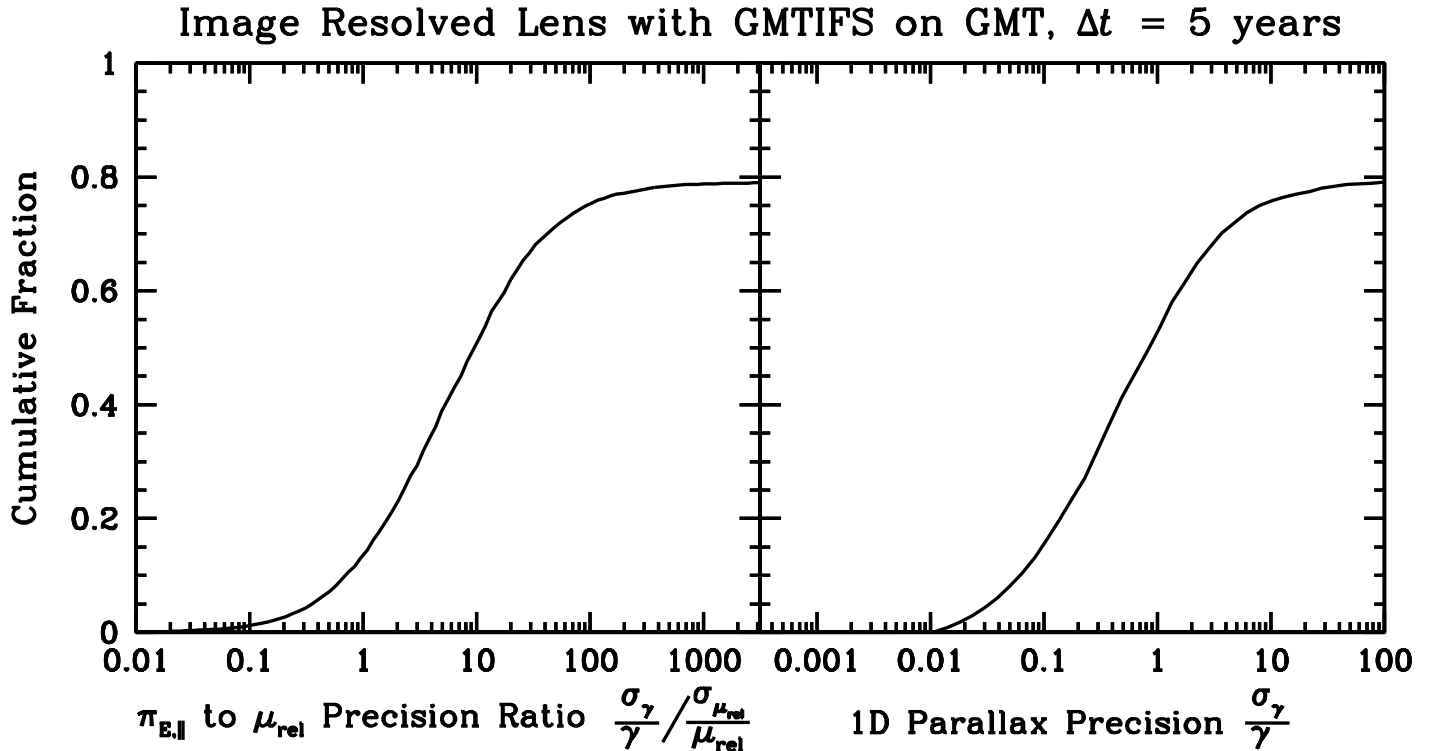


Figure 8. CDF of the ratio of the fractional precision of the one-dimensional parallax to that of the vector proper motion (left) and of the fractional precision of γ alone (right). In general the one-dimension parallax $\pi_{E,||}$ is known to poorer precision than is μ_{rel} . Only $\sim 14\%$ of events would have lens masses known to $\leq 10\%$ using this method, under my assumptions.

Henderson for his inspiration, and Jennifer van Saders and Benjamin Shappee for use of their air mattress. This material is based in part upon work supported by the National Science Foundation (NSF) Graduate Research Fellowship Program under Grant No. DGE-0822215, and an international travel allowance through the Graduate Research Opportunities Worldwide, taken to Cheongju, Korea. Any opinions, findings, and conclusions or recommendations expressed in this material are those of the author and do not necessarily reflect the views of the NSF. I recognize the direct support of The Ohio State University through a Distinguished University Fellowship. This research has made use of the Exoplanet Orbit Database and the Exoplanet Data Explorer at exoplanets.org.

REFERENCES

- Atwood, B., O'Brien, T. P., Colarosa, C., et al. 2012, in Society of Photo-Optical Instrumentation Engineers (SPIE) Conference Series, Vol. 8446, Society of Photo-Optical Instrumentation Engineers (SPIE) Conference Series
- Baraffe, I., Chabrier, G., Allard, F., & Hauschildt, P. H. 1998, *A&A*, 337, 403
- . 2002, *A&A*, 382, 563
- Batista, V., Gould, A., Dieters, S., et al. 2011, *A&A*, 529, A102
- Batista, V., Beaulieu, J.-P., Gould, A., et al. 2014, *ApJ*, 780, 54
- Bennett, D. P., Anderson, J., Bond, I. A., Udalski, A., & Gould, A. 2006, *ApJ*, 647, L171
- Bennett, D. P., Anderson, J., & Gaudi, B. S. 2007, *ApJ*, 660, 781
- Bond, I. A., Abe, F., Dodd, R. J., et al. 2001, *MNRAS*, 327, 868
- Bond, I. A., Udalski, A., Jaroszyński, M., et al. 2004, *ApJ*, 606, L155
- Bozza, V. 2000, *A&A*, 355, 423
- Cardelli, J. A., Clayton, G. C., & Mathis, J. S. 1989, *ApJ*, 345, 245
- Cassan, A., Kubas, D., Beaulieu, J.-P., et al. 2012, *Nature*, 481, 167
- Chung, S.-J., Han, C., Park, B.-G., et al. 2005, *ApJ*, 630, 535
- Dong, S., Gould, A., Udalski, A., et al. 2009, *ApJ*, 695, 970
- Duquenois, A., & Mayor, M. 1991, *A&A*, 248, 485
- Erdl, H., & Schneider, P. 1993, *A&A*, 268, 453
- Fischer, D. A., & Marcy, G. W. 1992, *ApJ*, 396, 178
- Gould, A. 2000, *ApJ*, 535, 928
- . 2014, ArXiv e-prints, arXiv:1408.0797
- Gould, A., Gaudi, B. S., & Han, C. 2003, *ApJ*, 591, L53
- Gould, A., Miralda-Escude, J., & Bahcall, J. N. 1994, *ApJ*, 423, L105
- Gould, A., Udalski, A., An, D., et al. 2006, *ApJ*, 644, L37
- Gould, A., Udalski, A., Monard, B., et al. 2009, *ApJ*, 698, L147
- Gould, A., Udalski, A., Shin, I.-G., et al. 2014, *Science*, 345, 46
- Han, C. 2006, *ApJ*, 638, 1080
- Han, C., & Gould, A. 1995a, *ApJ*, 449, 521
- . 1995b, *ApJ*, 447, 53
- Han, C., Udalski, A., Choi, J.-Y., et al. 2013, *ApJ*, 762, L28
- Hardy, S. J., & Walker, M. A. 1995, *MNRAS*, 276, L79
- Henderson, C. B., Gaudi, B. S., Han, C., et al. 2014a, *ApJ*, 794, 52
- Henderson, C. B., Park, H., Sumi, T., et al. 2014b, *ApJ*, 794, 71
- Holtzman, J. A., Watson, A. M., Baum, W. A., et al. 1998, *AJ*, 115, 1946
- Hwang, K.-H., Choi, J.-Y., Bond, I. A., et al. 2013, *ApJ*, 778, 55
- Ida, S., & Lin, D. N. C. 2005, *ApJ*, 626, 1045
- Janczak, J., Fukui, A., Dong, S., et al. 2010, *ApJ*, 711, 731
- Kappler, N., Kappler, L., Poteet, W. M., et al. 2012, in Society of Photo-Optical Instrumentation Engineers (SPIE) Conference Series, Vol. 8444, Society of Photo-Optical Instrumentation Engineers (SPIE) Conference Series
- Kennedy, G. M., & Kenyon, S. J. 2008, *ApJ*, 673, 502
- Kim, S.-L., Park, B.-G., Lee, C.-U., et al. 2010, in Society of Photo-Optical Instrumentation Engineers (SPIE) Conference Series, Vol. 7733, Society of Photo-Optical Instrumentation Engineers (SPIE) Conference Series
- Kim, S.-L., Park, B.-G., Lee, C.-U., et al. 2011, in Society of Photo-Optical Instrumentation Engineers (SPIE) Conference Series, Vol. 8151, Society of Photo-Optical Instrumentation Engineers (SPIE) Conference Series
- Krisciunas, K., & Schaefer, B. E. 1991, *PASP*, 103, 1033
- Lada, C. J. 2006, *ApJ*, 640, L63
- Laney, C. D., Joner, M. D., & Pietrzyński, G. 2012, *MNRAS*, 419, 1637
- Lissauer, J. J. 1987, *Icarus*, 69, 249
- Majewski, S. R., Zasowski, G., & Nidever, D. L. 2011, *ApJ*, 739, 25

- McGregor, P. J., Bloxham, G. J., Boz, R., et al. 2012, in Society of Photo-Optical Instrumentation Engineers (SPIE) Conference Series, Vol. 8446, Society of Photo-Optical Instrumentation Engineers (SPIE) Conference Series
- Nataf, D. M., Gould, A., Fouqué, P., et al. 2013, *ApJ*, 769, 88
- Nidever, D. L., Zasowski, G., & Majewski, S. R. 2012, *ApJS*, 201, 35
- Peale, S. J. 1997, *Icarus*, 127, 269
- Poteet, W. M., Cauthen, H. K., Kappler, N., et al. 2012, in Society of Photo-Optical Instrumentation Engineers (SPIE) Conference Series, Vol. 8444, Society of Photo-Optical Instrumentation Engineers (SPIE) Conference Series
- Raghavan, D., McAlister, H. A., Henry, T. J., et al. 2010, *ApJS*, 190, 1
- Sumi, T., Abe, F., Bond, I. A., et al. 2003, *ApJ*, 591, 204
- Sumi, T., Bennett, D. P., Bond, I. A., et al. 2010, *ApJ*, 710, 1641
- Tsapras, Y., Street, R., Horne, K., et al. 2009, *Astronomische Nachrichten*, 330, 4
- Udalski, A. 2003, *AcA*, 53, 291
- Yee, J. C., Shvartzvald, Y., Gal-Yam, A., et al. 2012, *ApJ*, 755, 102
- Zheng, Z., Flynn, C., Gould, A., Bahcall, J. N., & Salim, S. 2004, *ApJ*, 601, 500